Inorganic Chemistry

Article

pubs.acs.org/IC

Regulation of the Rate of Dinucleation of a Monocopper(I) Complex Containing Bipyrimidine Rotary Units by Restricted Double Pyrimidine Rotation

Yohei Hattori, Michihiro Nishikawa,[†] Tetsuro Kusamoto, Shoko Kume,*[,‡] and Hiroshi Nishihara*

Department of Chemistry, School of Science, The University of Tokyo, 7-3-1 Hongo, Bunkyo-ku, Tokyo 113-0033, Japan

Supporting Information

ABSTRACT: New copper(I) complexes with coordinated 2-(4′-methyl)pyrimidinyl moieties were fabricated, and the isomerism of their pyrimidine ring linkage was investigated. The ligands bis[2-(diphenylphosphino)phenyl] ether (DPEPhos) and 4,4′-dimethyl-2,2′-bipyrimidine (dmbpm) were used to synthesize a heteroleptic copper(I) complex, $[Cu^{I}(DPEPhos)(dmbpm)]\cdot BF_4$ (**1**·BF_4), and a dinuclear copper(I) complex, $[(Cu^{I})_2(DPEPhos)_2(\mu\text{-dmbmp})](BF_4)_2$ [**2**·$(BF_4)_2$]. The X-ray crystallographic structures, UV−vis absorption spectra, and luminescence properties of the complexes were analyzed. The thermodynamic and kinetic aspects of the isomerism of **1**·BF_4 were examined by variable-temperature NMR. Double pyrimidine ring rotation was found to be restricted sterically by the bulky DPEPhos ligands. This limited the number of the possible isomers: **1**·BF_4 showed only isomers with either one (*io* isomer) or both (*oo* isomer) of the two methyl groups positioned away from the copper center, while dinuclear **2**·$(BF_4)_2$ was only found as a symmetric (*io*−*io*) isomer, with each of the two methyl groups positioned toward different copper centers. The addition of $[Cu(MeCN)_2(DPEPhos)]$ (**3**·BF_4) allowed both isomers of **1**·BF_4 to form **2**·$(BF_4)_2$, although at different rates and via different pathways, which were analyzed using time-dependent UV−vis spectroscopy. The *io* isomer dinucleated more quickly than the *oo* isomer owing to it being able to form **2**·$(BF_4)_2$ (i) without bond dissociation and (ii) without a sterically congested *ii* configuration around the copper center. In contrast, *oo*-**1**·BF_4 required (i) recombination of the bipyrimidine coordination bonds or (ii) formation of a product with higher thermodynamic energy, unsymmetric (*ii*−*oo*) **2**·$(BF_4)_2$. These findings are interpreted as demonstrating a novel kinetic property: a conversion rate determined by pyrimidine ring inversion.

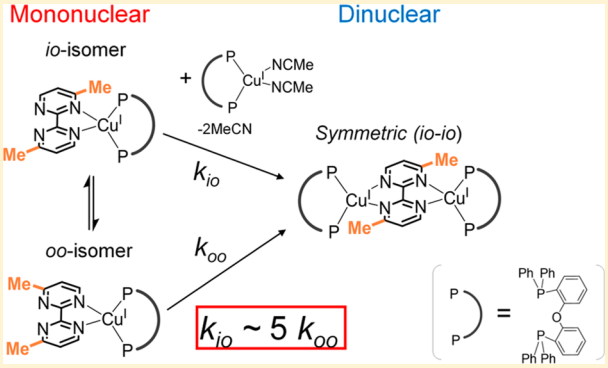

INTRODUCTION

Multistable molecules that show switchable structures and properties are potentially useful in stimuli-responsive molecule-based materials and devices.[1] Copper complexes can form dynamic multistable molecular systems: labile Cu^{I}−N coordination bonds in copper imine complexes enable reconstruction of the molecular structure by external stimuli, such as light and redox reactions.[2]

We have previously developed a pyridylpyrimidine-ligated copper(I) complex system that functions as a molecular rotor[3] (Figure 1). The pyrimidine ring in the ligand can rotate via dissociation and reconstruction of the Cu−N bond. Unsymmetric substitution at the 4 position of the pyrimidine ring affords two linkage isomers. In solution, these isomers interconvert through rotation of the pyrimidine ring and reach the equilibrium state shown in Figure 1, where the notation of inner (*i*) and outer (*o*) isomers indicates the direction relative to the copper center of the methyl group on the pyrimidine ring. The two isomers have different steric congestion within the coordination sphere around the copper(I) center. Steric congestion in complexes of copper with bis[2-(diphenylphosphino)phenyl] ether (DPEPhos) can influence

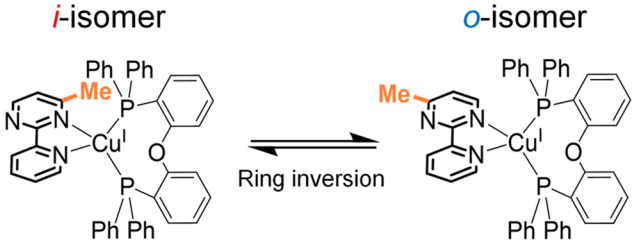

Figure 1. Two linkage isomers [inner (*i*) and outer (*o*)] of a pyridylpyrimidine-ligated copper(I) complex. The two DPEPhos−copper(I) complex isomers showed different lifetimes and heat sensitivities of luminescence.

the luminescence properties of the complexes[4] and can induce differences between the two luminescence lifetimes of the two isomers. Therefore, rotational isomerization can enable dual luminescence.[3b] Our previous work has developed complexes with unusual properties induced by rotational isomerization,

Received: September 27, 2013
Published: March 5, 2014

 © 2014 American Chemical Society dx.doi.org/10.1021/ic500074c | *Inorg. Chem.* 2014, 53, 2831−2840

Scheme 1. Synthesis of $1{\cdot}BF_4$ and $2{\cdot}(BF_4)_2$

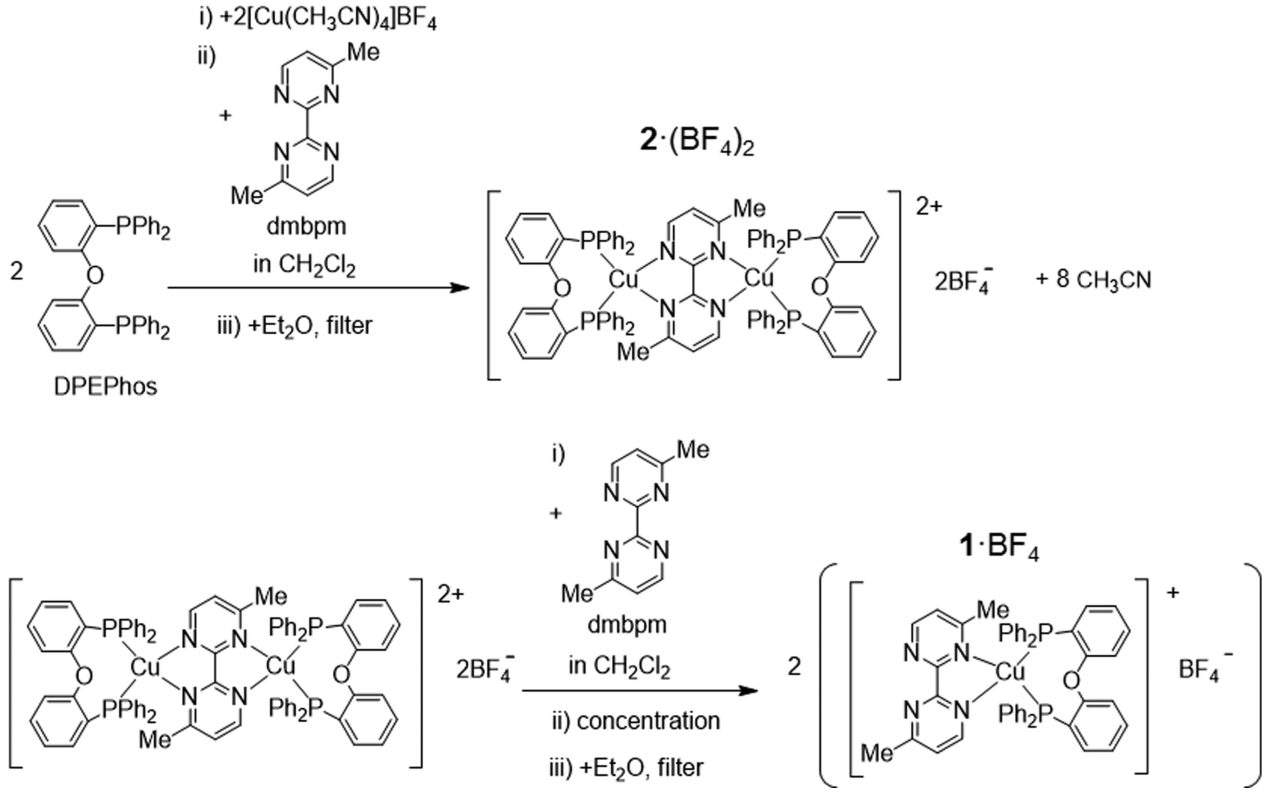

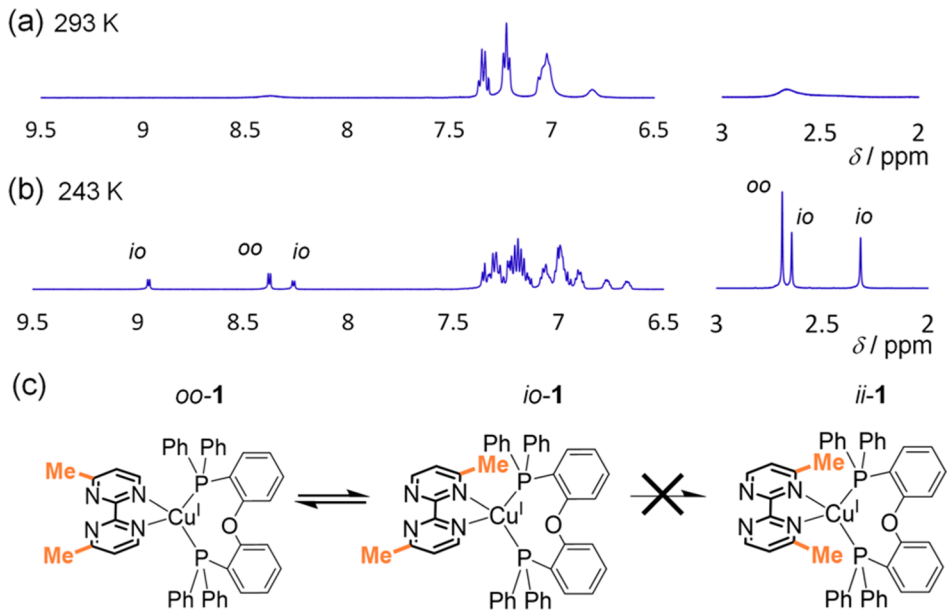

Figure 2. ^{1}H NMR spectra of $1{\cdot}BF_4$ in CD_2Cl_2 at (a) 293 and (b) 243 K. (c) Equilibrium between *oo*-1^+ and *io*-1^+.

such as a rest potential change[3c] and intramolecular electron transfer.[3d] We have shown that such systems can be applied to molecular rotor machinery.[3e,f] Rotation can also be driven by light.[3g]

This study focuses on dinucleation of a copper complex with pyrimidine rotors. The integration of two rotational units is expected to allow the development of more diverse properties, which have not been achieved previously using mononuclear complexes. The degree of correlation between the two rotating behaviors is dominated by the structure of the molecule; the degree of interaction between the two copper centers would be switchable by pyrimidine rotation.

Rotational isomerism in the mononuclear system is also expected to affect the kinetics of dinucleation. The mononuclear two-rotator isomers (*i* and *o* isomers) should behave differently, and their different mechanisms of dinucleation should show different rate constants. Such differences may enable the copper complexes to act as a new class of reaction regulators at the single-molecular level. The regulation of chemical reactions at a molecular level, such as the on−off

dx.doi.org/10.1021/ic500074c | Inorg. Chem. 2014, 53, 2831−2840

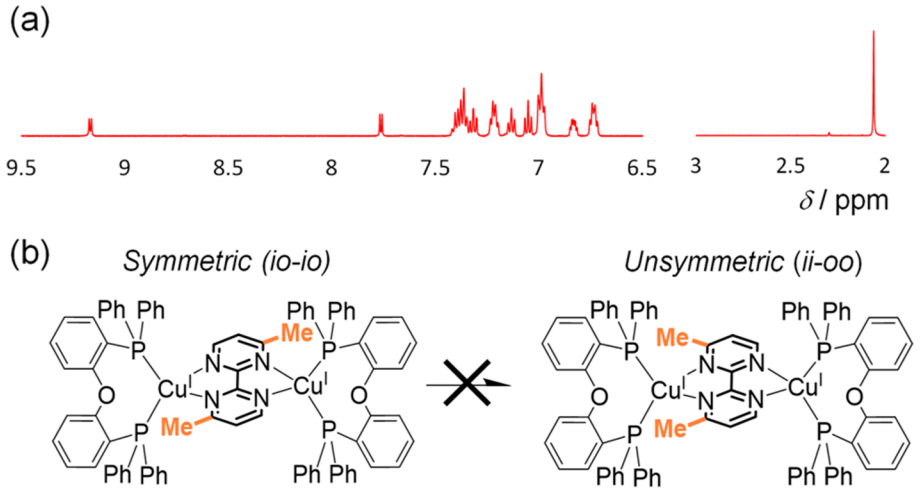

Figure 3. (a) ^{1}H NMR spectrum of **2**·$(BF_4)_2$ in CD_2Cl_2 at 293 K. (b) Symmetric (*io*–*io*) structure of **2**·$(BF_4)_2$.

switching of a catalytic reaction, has attracted much interest for its potential use in enzyme mimicking and artificial reaction control.[5]

This work reports the study of a mononuclear copper(I) complex, [Cu^I(DPEPhos)(dmbpm)]·BF_4 (**1**·BF_4; dmbpm = 4,4′-dimethyl-2,2′-bipyrimidine) and a dinuclear copper(I) complex, [$(Cu^I)_2$(DPEPhos)$_2$(μ-dmbpm)]$(BF_4)_2$ [**2**·$(BF_4)_2$]. In $\mathbf{2}^{2+}$, the dmbpm ligand bridges the two copper(I) centers within a short distance, allowing the centers to influence each other.[6] This ligand also allows linkage isomerism via pyrimidine rotation. ^{1}H NMR and X-ray crystallography studies indicated that steric hindrance by DPEPhos inhibited rotation of the pyrimidine rings, affording a limited number of isomers. The kinetic and thermodynamic properties of rotational isomerization were investigated to calculate the rate of pyrimidine rotation. Spectroscopic study and density functional theory (DFT) calculation assessed the steric effects of the methyl groups on the luminescence and stability of the complexes. The rate of formation of the dinuclear complex was isomer-dependent; therefore, an equilibrated mixture of the two mononuclear isomers showed a dual reaction rate. This study discloses a novel property attributable to pyrimidine rotational isomerization.

RESULTS AND DISCUSSION

Synthesis. Dinuclear **2**·$(BF_4)_2$ was synthesized by mixing DPEPhos, [$Cu(MeCN)_4$]BF_4, and dmbpm in a 2:2:1 molar ratio in dichloromethane (Scheme 1). Recrystallization by the addition of diethyl ether to the reaction mixture yielded a bright-orange powder (96% yield). Mononuclear **1**·BF_4 was synthesized by adding excess dmbpm to **2**·$(BF_4)_2$ in dichloromethane. The addition of diethyl ether to the concentrated dichloromethane solution yielded pure **1**·BF_4 as a yellow powder (84% yield). Recrystallization from a dilute dichloromethane solution of **1**·BF_4 gave a mixture of **1**·BF_4 and **2**·$(BF_4)_2$. This disproportionation occurred presumably due to the lower solubility of **2**·$(BF_4)_2$.

^{1}H NMR Study. ^{1}H NMR spectra of **1**·BF_4 in CD_2Cl_2 at room temperature show broad signals, demonstrating that interconversion between the isomers occurred on a time scale comparable to that of ^{1}H NMR (Figure 2a). At 243 K, two sets of signals appeared: two peaks at δ 2.64 and 2.32 were attributed to methyl protons (Figure 2b) of the *io* isomer, which showed both inner and outer methyl groups, and a signal at δ 2.69 was ascribed to methyl protons of the *oo* isomer. Compared with the signal from the *oo* isomer, the signal from the *i*-methyl group was shifted more upfield than that from the *o*-methyl group owing to the shielding effects of the DPEPhos ligand.[3b] The existence of the *oo* isomer (not the *ii* isomer) was also confirmed by the crystal structure (vide infra). The ratio of the *oo* isomer to the *io* isomer was 5:6 in CD_2Cl_2. No *ii* isomer was observed (Figure 2c).

2·$(BF_4)_2$ formed only a symmetric (*io*–*io*) isomer, which had the two methyl groups each directed oppositely toward a different copper center (Figure 3). The symmetric structure was also confirmed by the crystal structure (vide infra). ^{1}H NMR spectra in solvents of varying polarity (e.g., CD_2Cl_2, $CDCl_3$, acetone-d_6, and methanol-d_4) did not show evidence of an unsymmetric (*ii*–*oo*) isomer.

Variable-temperature ^{1}H NMR spectra of **1**·BF_4 in CD_2Cl_2 and acetone-d_6 were measured at 193–293 K. The *oo*:*io* ratio at each temperature was calculated by integration of the pyrimidine proton signals. The broad spectra acquired at high and low temperatures were excluded from thermodynamic analyses. van't Hoff plots were generated on the basis of the logarithm of [*oo* isomer]/[*io* isomer] versus reciprocal temperature (Figures S1a and S2a and Tables S1 and S2 in the Supporting Information , SI). The linear region of the plots was regarded as an equilibrium state, and the thermodynamic parameters were calculated from the temperature dependence of an equilibrium constant $K_{oo/io}$. The changes in both the enthalpy and entropy (ΔH and ΔS) for the transition from the *io* isomer to the *oo* isomer were small (Table 1).

The rate of inversion from the *io* isomer to the *oo* isomer was determined by fitting the experimental ^{1}H NMR spectra (Figures S1b and S2b in the SI). The aromatic 6-H signals on the pyrimidine ring were used for the simulations. As an example, in a CD_2Cl_2 solution at 253 K, they were at δ 8.95 and 8.27 for the *io* isomer and at δ 8.38 for the *oo* isomer. Equilibrium constants determined from the van't Hoff plots were used for simulation analysis. Arrhenius plots were drawn setting the rate constant $k_{io\rightarrow oo}$ as the rate constant for inversion from the *io* isomer to the *oo* isomer (Figures S1c and S2c in the SI). The kinetic parameters were calculated from the slope and intercept of a linear approximation to the Arrhenius plots. Activation energies (E_a) were estimated to be 89.5 kJ mol^{-1} in acetone-d_6 and 96.2 kJ mol^{-1} in CD_2Cl_2 (Table 1). The former

dx.doi.org/10.1021/ic500074c | Inorg. Chem. 2014, 53, 2831–2840

Table 1. Thermodynamic and Kinetic Parameters of the *io*–*oo* Isomerization of 1^+

parameter	1^+ in CD_2Cl_2	1^+ in acetone-d_6
$\Delta H_{io\rightarrow oo}$/kJ mol^{-1} [a]	0.6	1.0
$\Delta S_{io\rightarrow oo}$/J K^{-1} mol^{-1} [b]	1.0	6.1
$\Delta G_{io\rightarrow oo}$/kJ mol^{-1} [c]	0.3	−0.8
$E_{aio\rightarrow oo}$/kJ mol^{-1} [d]	96.2	89.5
log(A) [e]	19.9	19.8
$k_{io\rightarrow oo(298\ K)}$/s^{-1} [f]	1.0×10^3	1.4×10^4
$k_{io\rightarrow oo(193\ K)}$/s^{-1} [g]	7.1×10^{-7}	9.7×10^{-5}

[a]Molar enthalpy change. [b]Molar entropy change. [c]Molar Gibbs free-energy change at 298 K. [d]Activation energy. [e]Common logarithm of the preexponential factor. [f]Rate constant at 298 K. [g]Rate constant at 193 K from *io*-1^+ to *oo*-1^+.

was 6.7 kJ mol^{-1} lower than the latter; this situation is probably due to two reasons. One reason is the difference of $\Delta G_{io\rightarrow oo}$; the *oo* isomer is more stabilized in acetone-d_6 by 1.1 kJ mol^{-1} than in CD_2Cl_2, which would be reflected in E_a. The second reason is related to the higher polarity and coordinating ability of acetone, which promotes dissociation of the nitrogen atom from the copper center to stabilize the transition state.[3a,h] This leads to a decrease of E_a in acetone. By extrapolation of the Arrhenius plot, $k_{io\rightarrow oo}$ values out of the range of simulation (298 and 193 K) were calculated ($k_{io\rightarrow oo(298\ K)} = 1.0 \times 10^3$ s^{-1} and $k_{io\rightarrow oo(193\ K)} = 7.1 \times 10^{-3}$ s^{-1} in CD_2Cl_2 and $k_{io\rightarrow oo(298\ K)} = 1.4 \times 10^4$ s^{-1} and $k_{io\rightarrow oo(193\ K)} = 9.7 \times 10^{-5}$ s^{-1} in acetone-d_6).

X-ray Structural Analysis. Single crystals of [*oo*-**1**]·BF_4·CH_2Cl_2 were obtained by diffusing hexane into a dichloromethane solution of **1**·BF_4 (Figure 4a and Table S3 in the SI).

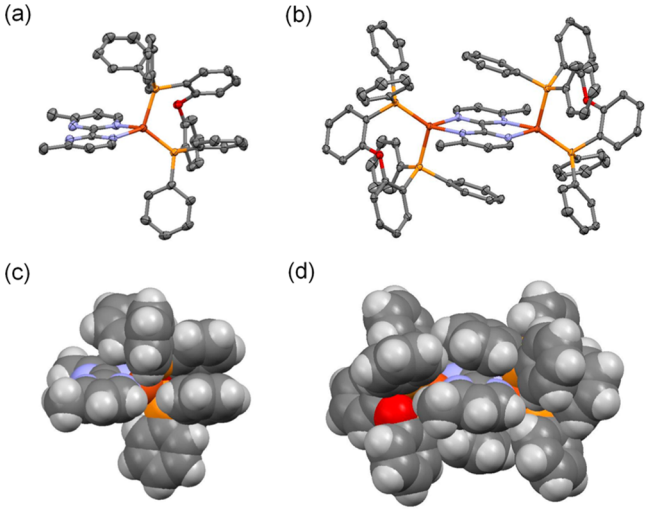

Figure 4. Molecular structures of crystalline (a) **1**·BF_4 and (b) **2**·$(BF_4)_2$ with thermal ellipsoids at the 50% probability level and (c and d) their respective space-filling models. Counteranions and solvent molecules are omitted for clarity.

Single crystals of [**2**]·$(BF_4)_2$·$(CH_2Cl_2)_2$ were obtained by diffusing diethyl ether into a dichloromethane solution of **2**·$(BF_4)_2$ (Figure 4b and Table S3 in the SI).

A crystal lattice of *oo*-**1** formed with a slightly distorted tetrahedral coordination environment; the two methyl groups were directed against the copper(I) center, so as to avoid a bulky DPEPhos ligand (Figure 4c). H–F contacts between the complex and BF_4 anion were 2.40–2.60 Å, and no intramolecular π–π-stacking or CH–π interactions were observed.

In the crystal of [**2**]·$(BF_4)_2$·$(CH_2Cl_2)_2$, bipyrimidine was sandwiched by two phenyl groups. The center of the bipyrimidine was 3.46 Å from the center of the phenyl group, indicative of a π–π-stacking interaction, as has been observed in other dinuclear complexes with terminal phosphines and bridging bipyrimidine.[7] Coordination around the copper(I) center of [**2**]·$(BF_4)_2$·$(CH_2Cl_2)_2$ was in a more distorted tetrahedral conformation than that of [*oo*-**1**]·BF_4·CH_2Cl_2. This was presumably due to formation of the π–π-stacking interaction or the avoidance of collision by the two DPEPhos ligands. Each of the two methyl groups at the 4 position was placed between one phenyl group and one *o*-phenoxy group. Opposite the methyl group, where a hydrogen atom at the 6 position is located, were two phenyl groups. These phenyl and *o*-phenoxy groups likely sterically inhibited rotation of the methylpyrimidine ring (Figure 4d).

Absorption and Emission Spectroscopy. UV–vis absorption spectra of **1**·BF_4 and **2**·$(BF_4)_2$ in dichloromethane were compared with those of model complexes [Cu(DPEPhos)(bpym)]BF_4 (**1′**·BF_4) and [Cu_2(DPEPhos)$_2$(μ-bpym)]$(BF_4)_2$ [**2′**·$(BF_4)_2$; bpym = 2,2′-bipyrimidine; Figure 5].[7b] The model complexes **1′** and **2′** were respectively similar

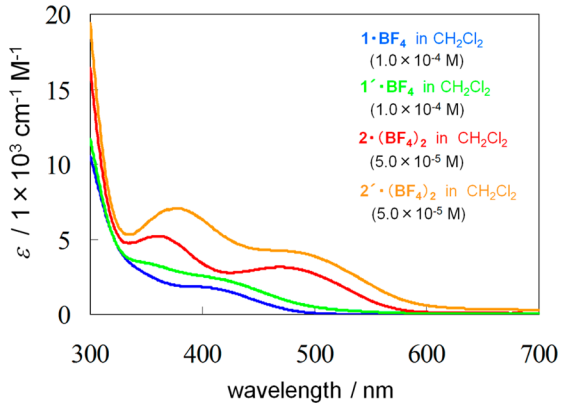

Figure 5. Absorption spectra of **1**·BF_4 (1.0×10^{-4} M, blue), **2**·$(BF_4)_2$ (5.0×10^{-5} M, red), **1′**·BF_4 (1.0×10^{-4} M, green), and **2′**·$(BF_4)_2$ (5.0×10^{-5} M, orange) in dichloromethane.

to the corresponding complexes **1** and **2**, although their bipyrimidine moieties lacked methyl groups. These complexes showed absorption bands in the near-UV and visible regions. **1**·BF_4 and **2**·$(BF_4)_2$ showed spectra similar to those of **1′**·BF_4 and **2′**·$(BF_4)_2$; the absorption coefficients of their absorption bands were slightly smaller than those of the corresponding model compounds. **1**·BF_4 showed an absorption shoulder at ca. 390 nm (molar extinction coefficient $\varepsilon = 1.85 \times 10^3$ M^{-1} cm^{-1}), and **2**·$(BF_4)_2$ displayed absorption maxima at 469 nm ($\varepsilon = 3.15 \times 10^3$ M^{-1} cm^{-1}) and 359 nm ($\varepsilon = 5.23 \times 10^3$ M^{-1} cm^{-1}). The assignment of the absorption bands is discussed in the DFT Calculation section (vide infra).

Corrected emission spectra of **1**·BF_4, **2**·$(BF_4)_2$, **1′**·BF_4, and **2′**·$(BF_4)_2$ in dichloromethane are shown in Figure S3a in the SI. **1**·BF_4 and **2**·$(BF_4)_2$ showed emission maxima ($\lambda_{max,em}$ = 673 and 739 nm, respectively) that were red-shifted (1.07×10^4 and 7.8×10^3 cm^{-1}) from the absorption shoulder of **1**·BF_4 and absorption maxima of **2**·$(BF_4)_2$ (λ_{abs} = 390 and 469 nm, respectively), while **1′**·BF_4 and **2′**·$(BF_4)_2$ showed emission maxima ($\lambda_{max,em}$ = ca. 750 and 780 nm, respectively) that were

dx.doi.org/10.1021/ic500074c | Inorg. Chem. 2014, 53, 2831–2840

more red-shifted (1.17×10^4 and 8.5×10^3 cm^{-1}) from the absorption shoulders of $\mathbf{1}'\cdot BF_4$ and $\mathbf{2}'\cdot(BF_4)_2$ (λ_{abs} = ca. 400 and 470 nm, respectively). $\mathbf{1}\cdot BF_4$, $\mathbf{2}\cdot(BF_4)_2$, $\mathbf{1}'\cdot BF_4$, and $\mathbf{2}'\cdot(BF_4)_2$ are thought to undergo geometrical changes from the ground state to the charge-transfer (CT) excited state similar to those shown by copper(I) (diimine)(diphosphine) complexes.[4,8] Larger Stokes shifts in $\mathbf{1}'\cdot BF_4$ and $\mathbf{2}'\cdot(BF_4)_2$ suggest a larger geometrical change because of the lack of steric hindrance of the methyl group directed toward the copper(I) atoms in the *io*- $\mathbf{1}\cdot BF_4$ and the symmetric *io*–*io* complex $\mathbf{2}\cdot(BF_4)_2$. $\mathbf{1}\cdot BF_4$ and $\mathbf{2}\cdot(BF_4)_2$ displayed stronger luminescence than their corresponding model complexes (Figure S3a in the SI). The relative luminescence quantum yields were $\phi = 1.1 \times 10^{-4}$ ($\mathbf{1}\cdot BF_4$), 4.2×10^{-5} ($\mathbf{2}\cdot(BF_4)_2$), 4×10^{-6} ($\mathbf{1}'\cdot BF_4$), and 4×10^{-6} ($\mathbf{2}'\cdot(BF_4)_2$). Rhodamine 6G was used as the quantum yield standard, assuming a value of 0.95 in ethanol.[9] These are explained by the fact that the steric methyl groups minimized the structural relaxation and raised the energy of the excited state, as shown in the emission spectral shift. In addition, the methyl groups would suppress the solvent-induced and exciplex quenching.[4a]

Both $\mathbf{1}\cdot BF_4$ and $\mathbf{2}\cdot(BF_4)_2$ displayed stronger luminescence in the solid state (powder; Figure 6 and S3b in the SI) than in solution. Their emission maxima and absolute luminescence quantum yields ϕ in the solid states were $\lambda_{max,em}$ = 587 nm and ϕ = 0.020 and $\lambda_{max,em}$ = 642 nm and ϕ = 0.035, respectively. The emission maxima were red-shifted 8.6×10^3 and 5.7×10^3 cm^{-1}, respectively, from the absorption maxima observed in solution. The luminescence of $\mathbf{1}'\cdot BF_4$ was weaker than those of the other complexes.

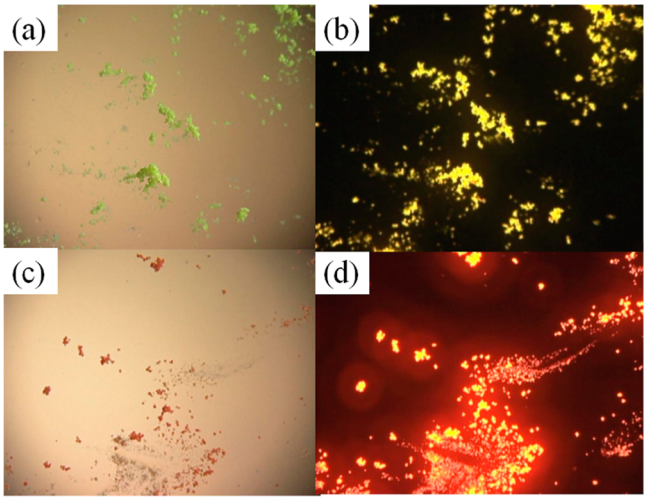

Figure 6. Fluorescent microscopy pictures of (a) $\mathbf{1}\cdot BF_4$ and (c) $\mathbf{2}\cdot BF_4$ and (b and d) their respective luminescence under blue-light excitation.

Electrochemistry. Cyclic voltammograms (CVs) were measured in dichloromethane with 0.1 M Bu_4NBF_4 as the supporting electrolyte; solutions of 2.0 mM $\mathbf{1}\cdot BF_4$ and 1.0 mM $\mathbf{2}\cdot(BF_4)_2$ were tested (Figure S4 in the SI). The CV of $\mathbf{1}\cdot BF_4$ showed an irreversible oxidation peak at 1.15 V vs Ag^+/Ag and an irreversible reduction peak at −1.76 V. The CV of $\mathbf{2}\cdot(BF_4)_2$ exhibited an irreversible oxidation peak at 1.33 V, a reversible reduction peak at −1.09 V, and an irreversible reduction peak at −1.66 V. $\mathbf{1}\cdot BF_4$ is more easily oxidized than $\mathbf{2}\cdot(BF_4)_2$ because $\mathbf{1}^+$ is a monocation and $\mathbf{2}^{2+}$ is a dication. Especially, two positively charged copper(I) atoms stabilized the one-electron reduction of $\mathbf{2}\cdot(BF_4)_2$, and the first reduction process became reversible. The redox sites of these compounds and the quantitative values of the redox potentials are discussed together with the calculated values in the following section.

DFT Calculation. The molecular and electronic structures of *oo*-$\mathbf{1}^+$, *io*-$\mathbf{1}^+$, *ii*-$\mathbf{1}^+$, and $\mathbf{2}^{2+}$ were investigated via ground-state DFT calculations using B3LYP[10] and M06[11] hybrid functionals. *ii*-$\mathbf{1}^+$ is an imaginary isomer that was not experimentally observed. The calculated structures of *oo*-$\mathbf{1}^+$ and $\mathbf{2}^{2+}$ were compared with those in their crystalline forms. The π–π stacking between the pyrimidine and the phenyl groups that appeared in the crystal $[\mathbf{2}]\cdot(BF_4)_2\cdot(CH_2Cl_2)_2$ was not reproduced by B3LYP, which does not include dispersive interactions, although the π–π stacking was retained using M06, which gives a good performance for the noncovalent interactions.

The summation of the electronic and thermal free energies of isomers of $\mathbf{1}^+$ was calculated to be *oo* = −80207.19 eV, *io* = −80207.05 eV, and *ii* = −80206.77 eV using B3LYP and *oo* = −80166.53 eV, *io* = −80166.51 eV, and *ii* = −80166.46 eV using M06. The per mole energies of the *io* and *ii* isomers relative to the *oo* isomer were +13.5 and +40.7 kJ mol^{-1}, respectively, using B3LYP and +2.4 and +7.2 kJ mol^{-1}, respectively, using M06. The order of the calculated ground-state energies, *oo* < *io* < *ii*, agreed with the experiments. The per mole energies of the *io* isomer relative to the *oo* isomer estimated from the ^{1}NMR results [1:1.2:0 in CD_2Cl_2 and 1:0.8:0 in acetone-d_6; the ratio of the *io* isomer is doubled because the *io* and *oi* isomers are the same (1.2 = 2 × 0.6, 0.8 = 2 × 0.4)] were +1.3 kJ mol^{-1} in CD_2Cl_2 and +2.3 kJ mol^{-1} in acetone-d_6, and the per mole energies of the *ii* isomer relative to the *oo* isomer should be ≫+10 kJ mol^{-1} in both solvents. Although the relative energy of the *io* isomer well agreed with the calculation using M06, the relative energy of the *ii* isomer estimated using M06 was too small. The calculated energy using B3LYP was large enough to exclude both the *io* and *ii* isomers.

The contour surfaces and calculated energies of selected molecular orbitals (LUMO+1, LUMO, HOMO, and HOMO−1) are shown in Figures 7 and S5 in the SI. For $\mathbf{1}^+$, three isomers formed similar electronic structures around the frontier orbitals; LUMO and LUMO+1 were centered mainly on dmbpm, and HOMO and HOMO−1 were mainly located at the copper and DPEPhos. LUMO and LUMO+1 of $\mathbf{2}^+$ exhibited electron density distributions similar to those of $\mathbf{1}^+$ and were mainly centered on the dmbpm ligand. HOMO and HOMO−1 of $\mathbf{2}^+$ were close to degenerate; they were expressed as bonding and antibonding combinations of molecular orbitals similar to the HOMO of $\mathbf{1}^+$, in which the electron density was distributed on copper and DPEPhos. Both HOMO and LUMO of $\mathbf{2}^{2+}$ were lower in energy than those of $\mathbf{1}^+$, which was confirmed by electrochemical measurements. The HOMO–LUMO gaps calculated by DFT are 3.3 eV (B3LYP) and 3.8 eV (M06) for $\mathbf{1}^+$ and 2.5 eV (B3LYP) and 3.0 eV (M06) for $\mathbf{2}^{2+}$. The values calculated using B3LYP are similar to $e\Delta E = e(E^{ox} - E_P^{red})$ estimated by cyclic voltammetry: 2.91 eV for $\mathbf{1}\cdot BF_4$ and 2.42 eV for $\mathbf{2}\cdot(BF_4)_2$, where E^{ox} is the reversible oxidation potential, E_P^{red} is the first reduction peak potential from cyclic voltammetry, and ΔE roughly indicates the electrochemical HOMO–LUMO gap. Although the values calculated using M06 are a little higher than the electrochemical values, they

dx.doi.org/10.1021/ic500074c | Inorg. Chem. 2014, 53, 2831−2840

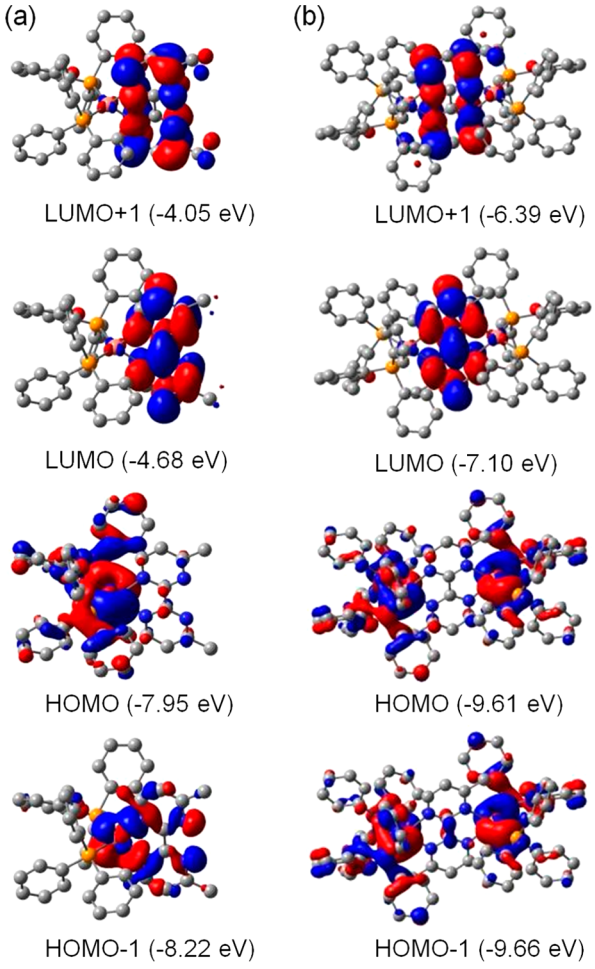

Figure 7. Selected molecular orbitals of (a) *oo*-$\mathbf{1}^{+}$ and (b) $\mathbf{2}^{2+}$ calculated using DFT (B3LYP).

also indicate a larger HOMO−LUMO gap for $\mathbf{1}\cdot BF_4$ than $\mathbf{2}\cdot(BF_4)_2$.

Visible absorption spectra were compared with the results from time-dependent DFT (TDDFT) using B3LYP. The main transitions are listed in Table S4 in the SI. The transitions from HOMO to LUMO and from HOMO−1 to LUMO+1 contributed considerably to absorption in $\mathbf{2}^{2+}$; absorption in *oo*-$\mathbf{1}^{+}$ and *io*-$\mathbf{1}^{+}$ showed significant contributions from the four transitions from each of HOMO and HOMO−1 to both LUMO and LUMO+1. Thus, the visible absorption bands of $\mathbf{1}^{+}$ and $\mathbf{2}^{2+}$ were interpreted as CT bands from the copper- and DPEPhos-based orbitals to the dmbpm-based orbitals. Calculations of the visible bands in similar copper complexes have also been similarly interpreted in previous works.[7b,12]

A smaller HOMO−LUMO gap was inferred to cause $\mathbf{2}^{2+}$ to display absorption bands at longer wavelengths than those shown by $\mathbf{1}^{+}$. The molecular orbitals in the divalent cation ($\mathbf{2}^{2+}$) were lower in energy than those in the monovalent cation ($\mathbf{1}^{+}$), in which the stronger electrostatic attraction between the cation and electrons stabilized the energy of the electrons. LUMO of $\mathbf{2}^{2+}$ was between the two copper ions, suggesting that the electrostatic interaction from the two positive charges was much stronger to LUMO than to HOMO (HOMO is localized on each copper ion and DPEPhos ligand). Therefore, the energy of LUMO decreased more greatly than that of HOMO, which led to the small HOMO−LUMO gap.

Time-Traced UV−vis Spectroscopic Analysis of the Formation of $\mathbf{2}\cdot(BF_4)_2$ from $\mathbf{1}\cdot BF_4$. The reaction kinetics of *io*-$\mathbf{1}^{+}$ and *oo*-$\mathbf{1}^{+}$ were next studied to elucidate isomer-dependent properties triggered by methylpyrimidine ring inversion. Dinucleation of $\mathbf{1}\cdot BF_4$ was chosen as a model reaction to examine because both isomers yielded the same product $[\mathbf{2}\cdot(BF_4)_2]$ upon the addition of [Cu(MeCN)$_2$(DPEPhos)]($\mathbf{3}\cdot BF_4$). The *io* and *oo* isomers of $\mathbf{1}^{+}$ were expected to behave differently during dinucleation and thus show different rate constants. *io*-$\mathbf{1}^{+}$ reacted with $\mathbf{3}^{+}$ to afford symmetric (*io*−*io*) $\mathbf{2}^{2+}$, while *oo*-$\mathbf{1}^{+}$ had two possible pathways: (i) it undergoes concerted rotation of the methylpyrimidine moiety during bond formation, furnishing (*io*−*io*) $\mathbf{2}^{2+}$; (ii) it first forms (*ii*−*oo*) $\mathbf{2}^{2+}$, which will rapidly isomerize to (*io*−*io*) $\mathbf{2}^{2+}$ upon warming to room temperature (Figure 8). Differences of reactivities between the *io* and *oo*

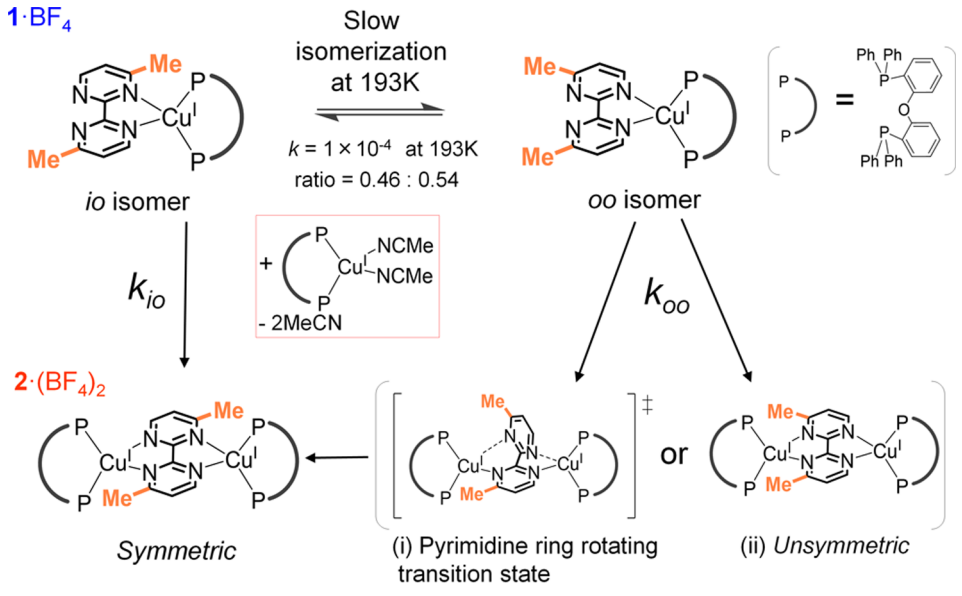

Figure 8. Reaction pathways for the formation of $\mathbf{2}\cdot(BF_4)_2$ from *oo*-$\mathbf{1}\cdot BF_4$ and *io*-$\mathbf{1}\cdot BF_4$ at 193 K.

dx.doi.org/10.1021/ic500074c | Inorg. Chem. 2014, 53, 2831−2840

isomers were observed at 193 K, which is just sufficient to prevent interconversion of the *io* and *oo* isomers. These tests and analyses found the coexistence of fast and slow reaction rates, which correspond to k_{io} and k_{oo}, respectively. Note that the quantitative production of (*io*−*io*) **2**·$(BF_4)_2$ was detected by UV−vis spectrometry and ^{1}H NMR when **3**·BF_4 was added to a solution of **1**·BF_4 at room temperature.

A 2.5 mL acetone solution of **1**·BF_4 was cooled sufficiently (to 193 K) to freeze interconversion of the *io* and *oo* isomers ($k_{io\rightarrow oo}$ = 9.7 × 10^{-5} s^{-1} estimated at 193 K in acetone by extrapolation of the Arrhenius plot; Figure S2c in the SI). A total of 1.08 equiv of **3**·BF_4 was added to this solution, and UV−vis absorption spectra were measured every 1 s (Figure 9a). After the reaction had reached completion (10 min), the

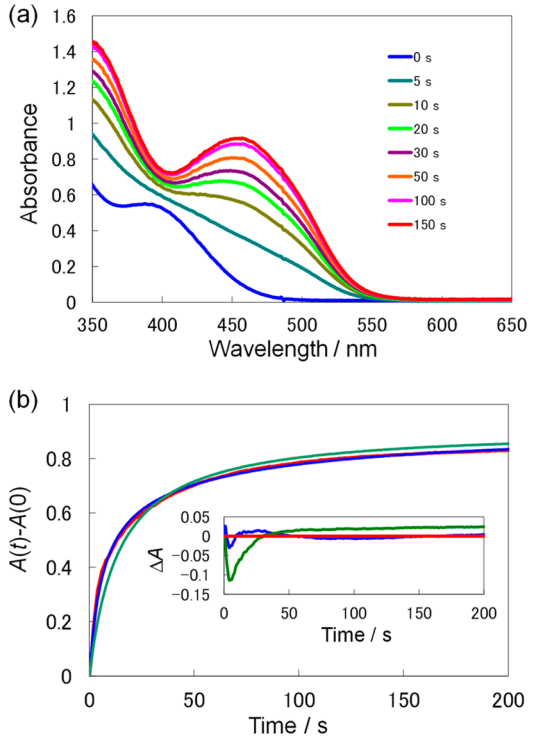

Figure 9. (a) Time-resolved absorption spectra during the formation of **2**·$(BF_4)_2$ from **1**·BF_4 at 193 K in acetone. (b) Time-dependent variation of absorbance $A(t) - A(0)$ at 470 nm. $A(t)$ indicates the absorbance at t seconds after the addition of **3**·BF_4 to the solution. Averaged experimental results (A_{exp}, red line), and fitting curves using eq 1 ($A_{eq\ 1}$, green line) and eq 2 ($A_{eq\ 2}$, blue line) . Inset in b: ΔA = $A_{exp} - A_{eq\ 1}$ (green line), $A_{exp} - A_{eq\ 2}$ (blue line), and $A_{exp} - A_{exp} = 0$ (red line).

spectra appeared similar to that of **2**·$(BF_4)_2$ at 193 K, indicating that **2**·$(BF_4)_2$ was indeed produced. The product from the *oo* isomer could be assigned as the symmetric (*io*−*io*) isomer or the unsymmetric (*ii*−*oo*) isomer (vide infra). The complete formation of symmetric **2**·$(BF_4)_2$ indicates that ring rotation, which is stopped in **1**·BF_4 at 193 K, was promoted by the addition of another copper center. Spectral differences between two periods of time after the addition of **3**·BF_4 to a **1**·BF_4 solution at 193 K were calculated and normalized at the maxima, and all of these graphs showed similar spectral shapes within the margin of error (Figure S6 in the SI). This indicates that *io*-$\mathbf{1}^+$ and *oo*-$\mathbf{1}^+$ showed negligibly different UV−vis absorption spectra in these experiments.

Time dependence of the absorbance at 470 nm during dinucleation was examined six times (Figure S7 in the SI). The six curves showed basically identical shapes with little discrepancy, indicating the repeatability of these experiments. The curves show apparent inflection points at around 5 s [around absorbance change $A(t) - A(0) \approx 0.4$]. Two model equations are proposed to interpret the experimental results:

$$d[\mathbf{2}^{2+}]/dt = k[\mathbf{1}^+][\mathbf{3}^+] \quad (1)$$

$$d[\mathbf{2}^{2+}]/dt = k_{io}[io\text{-}\mathbf{1}^+][\mathbf{3}^+] + k_{oo}[oo\text{-}\mathbf{1}^+][\mathbf{3}^+] \quad (2)$$

Equation 1 is a rate equation for a one-component second-order reaction, and eq 2 is that for a two-component (k_{io} and k_{oo}) second-order reaction. Equation 1 is a special case of eq 2 for $k_{io} = k_{oo}$. The equilibrium constants derived from ^{1}H NMR and the absorption coefficients obtained from UV−vis absorption spectra at 193 K were used as fixed parameters. The average of the six curves (red line, Figure 9b) is fitted by these equations, with the optimized fitting curve calculated using eq 1 (k = 337 M^{-1} s^{-1}; green line, Figure 9b) showing an inferior fit to that calculated using eq 2 ({k_{io}, k_{oo}} = {1054 M^{-1} s^{-1}, 216 M^{-1} s^{-1}}; blue line, Figure 9b). The differences between the simulation and experimental results were quantified using residual sums of squares; these were 0.1701 for eq 1 and 0.0090 for eq 2 (see also Figure S8 in the SI for a further comparison of eqs 1 and 2). These results strongly indicate that the reaction is rationalized by eq 2, i.e., that the reaction involves two second-order processes with different rate constants, k_{io} and k_{oo}. The two obtained kinetic constants, 1054 and 216 M^{-1} s^{-1}, were assignable to k_{io} and k_{oo}, respectively. *io*-$\mathbf{1}^+$ simply reacted with $\mathbf{3}^+$ to afford symmetric (*io*−*io*) $\mathbf{2}^{2+}$, while *oo*-$\mathbf{1}^+$ required a greater activation energy (i) to allow rotation of the pyrimidine ring or (ii) to accept a less stable dinuclear (*ii*−*oo*) $\mathbf{2}^{2+}$ configuration, which yielded the smaller rate constant. Dinucleation from *io*-$\mathbf{1}^+$ occurred 5 times more quickly than the reaction from *oo*-$\mathbf{1}^+$. This is a novel property change triggered by rotational isomerization: the reaction pathways were affected by isomerization.

We proposed two possible mechanisms for dinucleation of *oo*-$\mathbf{1}^+$. One possible mechanism is the direct formation of symmetric (*io*−*io*) $\mathbf{2}^{2+}$. In this pathway, the exergonic dinucleation reaction assists ring rotation. In the postulated transition state (Figure 8, hypothetic transition state), the bond formation energy of a new Cu−N bond compensates for a considerable proportion of the dissociation energy of one of the Cu−N bonds. As a result, one pyrimidine ring is released and can rotate to form symmetric (*io*−*io*) $\mathbf{2}^{2+}$. The formation of unsymmetric (*ii*−*oo*) $\mathbf{2}^{2+}$ is the other possible mechanism. In this pathway, the explanation of ring rotation is not needed, while *oo*-$\mathbf{1}^+$ has to form a (*ii*−*oo*) $\mathbf{2}^{2+}$ intermediate, which would have a congested structure with more steric restraints than *ii*-$\mathbf{1}^+$.

We attempted to monitor the dinucleation reaction at 193 K by ^{1}H NMR spectroscopy in an effort to reveal which pathway could interpret the reaction. The acetone-d_6 solution of **1**·BF_4 was mixed with 1.2 equiv of **3**·BF_4 in acetone-d_6 at 179 K using a liquid N_2−acetone bath, and the ^{1}H NMR spectrum was quickly obtained at 193 K (Figure S9a in the SI). The protons on dmbpm showed only one set of signals at δ 9.68 (2H), 7.95 (2H), and 2.15 (6H) in the spectrum. The chemical shifts of the signals became identical with that of the (*io*−*io*) $\mathbf{2}^{2+}$ isomer cooled to 193 K (Figure S9b in the SI).[13] These results support the direct formation of symmetric (*io*−*io*) $\mathbf{2}^{2+}$. Thus, the

dx.doi.org/10.1021/ic500074c | Inorg. Chem. 2014, 53, 2831−2840

concerted ring rotation and Cu−N bond formation mechanism is likely from ^{1}H NMR observation.

CONCLUSIONS

Mono- and dinuclear DPEPhos−copper(I) complexes that incorporated dmbpm ligands were successfully synthesized. The dinuclear complex assumed only a symmetric (*io*−*io*) structure, while the mononuclear complex showed *oo* and *io* isomers. The absence of a mononuclear *ii* isomer was also supported by DFT calculations. Crystal structural analysis suggested that rotation of the pyrimidine ring is strongly affected by steric hindrance from the DPEPhos ligands. These complexes showed CT bands in the visible region and displayed luminescence. The absorption and luminescence spectra were considerably influenced by the presence of the methyl groups. Spectroscopic differences between the mono- and dinuclear complexes were interpreted with the support of TDDFT calculations and electrochemical tests. Formation of the dinuclear copper complex by the addition of a copper source to the mononuclear complex was found to have two kinetic components. The faster reaction rate was attributed to the *io* isomer and the slower rate to the *oo* isomer because the *oo* isomer required (i) *oo* → *io* inversion before it could form the symmetric (*io*−*io*) isomer or (ii) formation of the unsymmetric (*ii*−*oo*) isomer, which only exists at low temperature.

These findings are interpreted as evidence of a new type of property: conversion by pyrimidine rotation; the restricted double pyrimidine rotation regulates the reaction rates of dinucleation. This study suggests that the present molecular rotor is a potential new reaction regulator at the single-molecular level.

EXPERIMENTAL SECTION

Materials. Tetrakis(acetonitrile)copper(I) tetrafluoroborate[14] ($[Cu(MeCN)_4]BF_4$) and $[Cu(MeCN)_2(DPEPhos)]$[15] (**3**·BF_4) were prepared according to reported methods. 4,4′-Dimethyl-2,2′-bipyrimidine (dmbpm)[16] was synthesized from 2-hydroxy-4-methylpyrimidine hydrochloride using a reported method for the synthesis of 2,2′-bipyrimidine.[17] $[Cu_2(DPEPhos)_2(\mu\text{-bpym})](BF_4)_2$ [**2′**·$(BF_4)_2$] and $[Cu(DPEPhos)(bpym)]BF_4$ (**1′**·BF_4) were prepared using modified literature procedures,[7b] as were **2**·$(BF_4)_2$ and **1**·BF_4. The complexes were characterized by ^{1}H NMR. Bis[2-(diphenylphosphino)phenyl] ether (DPEPhos), 2-hydroxy-4-methylpyrimidine hydrochloride, and spectroscopy-grade acetone were from Wako Pure Chemical Industries, Ltd.

Synthesis of $[Cu_2(DPEPhos)_2(\mu\text{-dmbpm})](BF_4)_2$ [2·$(BF_4)_2$]. The bipyrimidine-bridged dinuclear copper complex **2**·$(BF_4)_2$ was synthesized using a modified literature procedure.[3b] $[Cu(MeCN)_4]BF_4$ (63.1 mg, 0.20 mmol) was added to DPEPhos (107.8 mg, 0.20 mmol) in 5 mL of CH_2Cl_2. dmbpm (18.6 mg, 0.10 mmol) in 5 mL of CH_2Cl_2 was added dropwise, and the reaction mixture was stirred for 30 min. Diethyl ether was added to precipitate the product as an orange solid, which was filtered and washed with diethyl ether (149.8 mg, 0.0958 mmol, 95.8% yield). ^{1}H NMR (500 MHz, CD_2Cl_2, 293 K, ^{1}H−^{1}H COSY spectrum is shown in Figure S10 in the SI): δ 9.17 (d, J = 5.4 Hz, 2H), 7.76 (d, J = 5.4 Hz, 2H), 7.42−7.34 (m, 12H), 7.32 (t, J = 7.6 Hz, 4H), 7.21 (q, 8H), 7.13 (t, J = 7.5 Hz, 4H), 7.05 (t, J = 7.5 Hz, 4H), 6.99 (t, 12H), 6.84 (m, 4H), 6.73 (q, 8H), 2.06 (s, 6H). ^{1}H NMR (500 MHz, acetone-d_6, 293 K): δ 9.34 (d, J = 5.4 Hz, 2H), 7.84 (d, J = 5.2 Hz, 2H), 7.47−7.43 (m, 8H), 7.37−7.31 (m, 16H), 7.24−7.12 (m, 20H), 6.98−6.88 (m, 12H), 2.26 (s, 6H). Elem anal. Calcd for **2**·$(BF_4)_2$·0.8CH_2Cl_2: C, 60.94; H, 4.18; N, 3.43. Found: C, 60.73; H, 4.54; N, 3.44. ESI-TOF-MS: m/z 1475.28 ($[2\cdot BF_4]^+$).

Synthesis of [Cu(DPEPhos)(dmbpm)]BF_4 (1·BF_4). The heteroleptic copper complex **1**·BF_4 was synthesized using a modified literature procedure.[3b] dmbpm (37.2 mg, 0.20 mmol) was added to **2**·$(BF_4)_2$ (156 mg, 0.10 mmol) in CH_2Cl_2 and stirred for 30 min. The product was obtained by concentration of the reaction mixture followed by precipitation by the addition of diethyl ether. A yellow solid was filtered and washed with diethyl ether (146.1 mg, 0.167 mmol, 83.5% yield). ^{1}H NMR (500 MHz, CD_2Cl_2, 243 K, *oo*/*io* ∼ 0.83, ^{1}H−^{1}H COSY spectrum is shown in Figure S11 in the SI): δ 8.95 (d, J = 5.0 Hz, 1H, *io*), 8.37 (d, J = 5.0 Hz, 2H, *oo*), 8.26 (d, J = 5.4 Hz, 1H, *io*), 7.36−6.87 (28H, *io*, 28H, *oo*), 6.77 (m, 2H, *io*), 6.66 (m, 2H, *oo*), 2.69 (s, 6H, *oo*), 2.64 (s, 3H, *io*), 2.32 (s, 3H, *io*). ^{1}H NMR (500 MHz, acetone-d_6, 233 K, *oo*/*io* ∼ 1.21): δ 9.06 (d, J = 5.0 Hz, 1H, *io*), 9.02 (d, J = 5.0 Hz, 1H, *io*), 8.81 (d, J = 5.2 Hz, 2H, *oo*), 7.71 (d, J = 4.9 Hz, 1H, *io*), 7.57 (d, J = 5.3 Hz, 1H, *io*, 2H, *oo*), 7.47−7.03 (26H, *io*, 26H, *oo*), 6.82−6.77 (2H, *io*), 6.68−6.64 (2H, *oo*), 2.68 (s, 6H, *oo*), 2.63 (s, 3H, *io*), 2.26 (s, 3H, *io*). Elem anal. Calcd for **1**·BF_4·0.1CH_2Cl_2: C, 62.66; H, 4.36; N, 6.34. Found: C, 62.47; H, 4.61; N, 6.09.

X-ray Structural Analysis. Yellow single crystals of [*oo*-**1**]·BF_4·CH_2Cl_2 were obtained by diffusing hexane into a dichloromethane solution of **1**·BF_4. Orange single crystals of [**2**]·$(BF_4)_2$·$(CH_2Cl_2)_2$ were obtained by diffusing diethyl ether into a dichloromethane solution of **2**·$(BF_4)_2$. Diffraction data for X-ray analysis were collected with an AFC10 diffractometer coupled with a Rigaku Saturn CCD system equipped with a rotating-anode X-ray generator producing graphite-monochromated Mo Kα radiation (λ = 0.7107 Å). Lorentz polarization and numerical absorption corrections were performed with the program *CrystalClear1.3.6*. Structures were solved by direct methods using *SIR92* software[18] and refined against F^2 using *SHELXL-97*.[19] *WinGX* software was used to prepare the material for publication.[20] The crystallographic data are listed in Table S3 in the SI. Crystal structure data (CIF; CCDC 959042 and 959043) are given in the SI and can be obtained free of charge via the Internet from The Cambridge Crystallographic Data Centre via www.ccdc.cam.ac.uk/data_request/cif.

Instruments. ^{1}H NMR spectra were recorded using a Bruker DRX500 spectrometer. The reported chemical shifts of the solvent residual peaks were used for calibration of the ^{1}H NMR spectra in CD_2Cl_2 (δ 5.32) and acetone-d_6 (δ 2.05).[21] Electrospray ionization time-of-flight mass spectrometry (ESI-TOF-MS) spectra were recorded using an LCT Micromass spectrometer. UV−vis absorption spectra of **1**·BF_4 and **2**·$(BF_4)_2$ in CH_2Cl_2 were recorded with a Jasco V-570 spectrometer. Solid-state luminescence images were measured under blue-light excitation using an Olympus BX51 fluorescence microscope. Steady-state emission spectra and relative quantum yields were measured with a Hitachi F-4500 spectrometer. Absolute photoluminescence quantum yields were measured with a Hamamatsu Photonics C9920-02G. Kinetic assessment of the synthesis of **2**·$(BF_4)_2$ from **1**·BF_4 and **3**·BF_4 at 193 K was conducted using UV−vis absorption spectra recorded in acetone in 1-cm-optical-path-length quartz cells using a Hewlett-Packard 8453 spectrometer equipped with a temperature controller (UNISOKU USP-203A). Electrochemical measurements were recorded with an ALS 650DT electrochemical analyzer (BAS. Co., Ltd.). The working electrode was a 0.3-mm-o.d. glassy carbon electrode, a platinum wire served as the auxiliary electrode, and the reference electrode was an Ag^+/Ag electrode (a silver wire immersed in 0.1 M Bu_4NClO_4/0.01 M $AgClO_4$/CH_3CN). The solutions were deoxygenated with pure argon prior to the electrochemical measurements.

Thermodynamic and Kinetic Analyses of ^{1}H NMR. **1**·BF_4 was analyzed using the aromatic ^{1}H NMR signals of the dmbpm moiety. The solution-state molar ratios of the isomers at several temperatures were determined from ^{1}H NMR signal integration. The broad spectra acquired at high and low temperature were excluded from thermodynamic analysis. The generated van't Hoff plots were based on an equilibrium constant corresponding to the value of [*oo*-isomer]/[*io*-isomer]. A rate of inversion from the *io* isomer to the *oo* isomer was determined via simulation analysis of the experimental ^{1}H NMR spectra. The simulations were performed using the iNMR software package. Equilibrium constants determined from the van't Hoff plot were used for simulation analysis. Arrhenius plots were drawn setting the rate constant k as the inversion rate constant. The rates of

dx.doi.org/10.1021/ic500074c | Inorg. Chem. 2014, 53, 2831−2840

inversion at different temperatures were calculated from the slope and intercept of the approximated Arrhenius plots.

Kinetic Assessment of the Synthesis of 2·$(BF_4)_2$ from Equimolar 1·BF_4 and 3·BF_4 at 193 K. In a 25 mL volumetric flask, 1·BF_4 (4.37 mg, 4.99 mmol) was dissolved in acetone to yield a yellow solution (2.00×10^{-4} M). 3·BF_4 (7.76 mg, 10 mmol) was dissolved in 0.5 mL of acetone; the concentration of this colorless solution was determined to be 1.80×10^{-2} M by titration with 1·BF_4 at room temperature. Using a volumetric pipet, 2.5 mL of a 1·BF_4 solution was added to a cell, stirred with a magnetic stirrer tip, and cooled to 193 K, and then the solution of 3·BF_4 (30 μL, equivalent to 2.15×10^{-4} M in 2.5 mL) was added by syringe at once. Absorption spectra and absorbance at 470 nm were recorded every 1 s.

Computational Details. DFT calculations were executed using the *Gaussian09* program package.[22] The geometries of the complexes were optimized without symmetry constraints using the crystal structure coordinate as the starting structure for *oo*-$\mathbf{1}^+$ and $\mathbf{2}^{2+}$ and employing minor changes (Me and H exchange) to the crystal structure of *oo*-$\mathbf{1}^+$ for *io*-$\mathbf{1}^+$ and *ii*-$\mathbf{1}^+$. Calculations were performed using Becke's three-parameter exchange functional with the Lee–Yang–Parr correlation functional (B3LYP)[10] and the hybrid functional of Truhlar and Zhao (M06),[11] together with the 6-31G basis set[23] for carbon, phosphorus, hydrogen, nitrogen, and oxygen atoms and the "double-ζ" quality LANL2DZ basis set[24] for the copper element. Cartesian coordinates of all of the optimized geometries are listed in the SI. Frequency calculations were carried out to ensure that the optimized geometries were minima on the potential energy surface, in which no imaginary frequencies were observed in any of the compounds. TDDFT calculations were performed using B3LYP to calculate the first 30 singlet transitions for *oo*-$\mathbf{1}^+$ and the first 20 singlet transitions for $\mathbf{2}^{2+}$.

■ ASSOCIATED CONTENT

Ⓢ Supporting Information

X-ray crystallographic data for [*oo*-**1**]·BF_4·CH_2Cl_2 and [**2**]·$(BF_4)_2$·$(CH_2Cl_2)_2$ in CIF format, crystal structure data, van't Hoff and Arrhenius plots, emission spectra, CVs, DFT and TDDFT, and kinetic assessment data. This material is available free of charge via the Internet at http://pubs.acs.org.

■ AUTHOR INFORMATION

Corresponding Authors

*E-mail: skume@hiroshima-u.ac.jp.
*E-mail: nisihara@chem.s.u-tokyo.ac.jp.

Present Addresses

[†]M.N.: Department of Materials and Life Science, Seikei Univeristy, 3-3-1 Kichijoji-kitamachi, Musashino-shi, 180-8633 Tokyo, Japan.
[‡]S.K.: Department of Chemistry, Graduate School of Science, Hiroshima University, 1-3-1 Kagamiyama, Higashi, Hiroshima 739-8526, Japan.

Notes

The authors declare no competing financial interest.

■ ACKNOWLEDGMENTS

This work was supported by Grants-in-Aid from MEXT of Japan [Grants 20750044, 20245013, and 21108002; area 2107 (Coordination Programming)], JST (Research Seeds Quest Program), the Global COE Program for Chemistry Innovation, and MERIT (Materials Education Program for the future leaders in Research, Industry, and Technology) in the MEXT Leading Graduate School Doctoral Program.

■ REFERENCES

(1) (a) Ikeda, T.; Nakano, M.; Yu, Y.; Tsutsumi, O.; Kanazawa, A. *Adv. Mater.* **2003**, *15*, 201–205. (b) Kobataka, S.; Takami, S.; Muto, H.; Ishikawa, T.; Irie, M. *Nature* **2007**, *446*, 778–781. (c) Green, J. E.; Choi, J. W.; Boukai, A.; Bunimovich, Y.; Johston-Halperin, E.; Delonno, E.; Luo, Y.; Sheriff, B. A.; Xu, K.; Shik Shin, Y.; Tseng, H.-R.; Stoddart, J. F.; Heath, J. R. *Nature* **2007**, *445*, 414–417. (d) Fraysee, S.; Coudret, C.; Launay, J.-P. *Eur. J. Inorg. Chem.* **2000**, 1581–1590. (e) Tanaka, Y.; Inagaki, A.; Akita, M. *Chem. Commun.* **2007**, 1169–1171.

(2) (a) Livoreil, A.; Sauvage, J.-P.; Armaroli, N.; Balzani, V.; Flamigni, L.; Ventura, B. *J. Am. Chem. Soc.* **1997**, *119*, 12114–12124. (b) Jiménez, M. C.; Dietrich-Buchecker, C.; Sauvage, J.-P. *Angew. Chem., Int. Ed.* **2000**, *39*, 3284–3287.

(3) (a) Nishikawa, M.; Kume, S.; Nishihara, H. *Phys. Chem. Chem. Phys.* **2013**, *15*, 10549–10565. (b) Nishikawa, M.; Nomoto, K.; Kume, S.; Inoue, K.; Sakai, M.; Fujii, M.; Nishihara, H. *J. Am. Chem. Soc.* **2010**, *132*, 9579–9581. (c) Nomoto, K.; Kume, S.; Nishihara, H. *J. Am. Chem. Soc.* **2009**, *131*, 3830–3831. (d) Kume, S.; Nomoto, K.; Kusamoto, T.; Nishihara, H. *J. Am. Chem. Soc.* **2009**, *131*, 14198–14199. (e) Kume, S.; Nishihara, H. *Chem. Commun.* **2011**, *47*, 415–417. (f) Kume, S.; Nishihara, H. *Dalton Trans.* **2011**, *40*, 2299–2305. (g) Nishikawa, M.; Nomoto, K.; Kume, S.; Nishihara, H. *J. Am. Chem. Soc.* **2012**, *134*, 10543–10553. (h) Nishikawa, M.; Nomoto, K.; Kume, S.; Nishihara, H. *Inorg. Chem.* **2013**, *52*, 369–380.

(4) (a) Cuttel, D. G.; Kuand, S.-M.; Fanwick, P. E.; McMillin, D. R.; Walton, R. A. *J. Am. Chem. Soc.* **2002**, *124*, 6–7. (b) Barbieri, A.; Accorsi, G.; Armaroli, N. *Chem. Commun.* **2008**, 2185–2193.

(5) (a) Broderick, E. M.; Guo, N.; Vogel, C. S.; Xu, C.; Sutter, J.; Miller, J. T.; Meyer, K.; Mehrkhodavandi, P.; Diaconescu, P. L. *J. Am. Chem. Soc.* **2011**, *133*, 9278–9281. (b) Schmittel, M.; De, S.; Pramanik, S. *Angew. Chem., Int. Ed.* **2012**, *51*, 3832–3836. (c) Imahori, T.; Yamaguchi, R.; Kurihara, S. *Chem.—Eur. J.* **2012**, *18*, 10802–10807. (d) Blanco, V.; Carlone, A.; Hänni, K. D.; Leigh, D. A.; Lewandowski, B. *Angew. Chem., Int. Ed.* **2012**, *51*, 5166–5169.

(6) (a) Concepcion, J. J.; Jurss, J. W.; Hoertz, P. G.; Meyer, T. J. *Angew. Chem., Int. Ed.* **2009**, *48*, 9473–9476. (b) Real, J.-A.; Bolvin, H.; Bousseksou, A.; Dworkin, A.; Kahn, O.; Varret, F.; Zarembowitch, J. *J. Am. Chem. Soc.* **1992**, *144*, 4650–4658. (c) Nitadori, H.; Takahashi, T.; Inagaki, A.; Akita, M. *Inorg. Chem.* **2012**, *51*, 51–62. (d) Shavaleev, N. M.; Accorsi, G.; Virgili, D.; Bell, Z. R.; Lazarides, T.; Calogero, G.; Armaroli, N.; Ward, M. D. *Inorg. Chem.* **2005**, *44*, 61–72.

(7) (a) Vogler, C.; Hausen, H.-D.; Kaim, W.; Kohlmann, S.; Kramer, H. E. A.; Rieker, J. *Angew. Chem., Int. Ed.* **1989**, *28*, 1659–1660. (b) Linfoot, C. L.; Richardson, P.; Hewat, T. E.; Moudam, O.; Forde, M. M.; Collins, A.; White, F.; Robertson, N. *Dalton Trans.* **2010**, *39*, 8945–8956. (c) Schwach, M.; Hausen, H.-D.; Kaim, W. *Chem.—Eur. J.* **1996**, *2*, 446–451.

(8) Vorontsov, I. V.; Graber, T.; Kovalevsky, A. Y.; Novozhilova, I. V.; Gembicky, M.; Chen, Y.-S.; Coppens, P. *J. Am. Chem. Soc.* **2009**, *131*, 6566–6573.

(9) Magde, D.; Wong, R.; Seybold, P. G. *Photochem. Photobiol.* **2002**, *75*, 327–334.

(10) Becke, A. D. *J. Chem. Phys.* **1993**, *98*, 5648–5652.

(11) Zhao, Y.; Truhlar, D. G. *Theor. Chem. Acc.* **2008**, *120*, 215–241.

(12) Sieger, M.; Vogler, C.; Klein, A.; Knödler, A.; Wanner, M.; Fiedler, J.; Záliš, S.; Snoeck, T. L.; Kaim, W. *Inorg. Chem.* **2005**, *44*, 4637–4643.

(13) The ^{1}H NMR signals of (*io*–*io*) $\mathbf{2}^{2+}$ at 193 K were broadened because of slow molecular fluctuation of DPEPhos. This phenomenon was also seen in previous researches of other copper(I) (diphosphine) (diimine) complexes. It might be possible that both *io*–*io* and *ii*–*oo* isomers showed the proton peaks in identical positions at 193 K; however, such a situation was not likely because the protons on the same position of the pyrimidine rings in the mononuclear complexes *io*-$\mathbf{1}^+$ and *oo*-$\mathbf{1}^+$ showed peaks with different chemical shifts.

(14) Merrill, C. L.; Wilson, L. J.; Thamann, T. J.; Loehr, T. M.; Ferris, N. S.; Woodruff, W. H. *J. Chem. Soc., Dalton Trans.* **1984**, 2207–2221.

(15) Armaroli, N.; Accorsi, G.; Holler, M.; Moudam, O.; Nierengarten, J.-F.; Zhou, Z.; Wegh, R. T.; Welter, R. *Adv. Mater.* **2006**, *18*, 1313.
(16) Mukkala, V.-M.; Sund, C.; Kwiatkowski, M.; Pasanen, P.; Högberg, M.; Kankare, J.; Takalo, H. *Helv. Chim. Acta* **1992**, *75*, 1621−1632.
(17) Nasielski, J.; Standaert, A.; Nasielski-Hinkens, R. *Synth. Commun.* **1991**, *21*, 901−906.
(18) Altomare, A.; Cascarano, G.; Giacovazzo, C.; Guagliardi, A.; Burla, M. C.; Polidori, G.; Camalli, M. *J. Appl. Crystallogr.* **1994**, *27*, 435.
(19) Sheldrick, G. M. *Acta Crystallogr., Sect. A* **2008**, *64*, 112−122.
(20) Farrugia, L. J. *J. Appl. Crystallogr.* **1999**, *32*, 837−838.
(21) Fulmer, G. R.; Miller, A. J. M.; Sherden, N. H.; Gottlieb, H. E.; Nudelman, A.; Stoltz, B. M.; Bercaw, J. E.; Goldberg, K. I. *Organometallics* **2010**, *29*, 2176−2179.
(22) Frisch, M. J.; Trucks, G. W.; Schlegel, H. B.; Scuseria, G. E.; Robb, M. A.; Cheeseman, J. R.; Scalmani, G.; Barone, V.; Mennucci, B.; Petersson, G. A.; Nakatsuji, H.; Caricato, M.; Li, X.; Hratchian, H. P.; Izmaylov, A. F.; Bloino, J.; Zheng, G.; Sonnenberg, J. L.; Hada, M.; Ehara, M.; Toyota, K.; Fukuda, R.; Hasegawa, J.; Ishida, M.; Nakajima, T.; Honda, Y.; Kitao, O.; Nakai, H.; Vreven, T.; Montgomery, J. A., Jr.; Peralta, J. E.; Ogliaro, F.; Bearpark, M.; Heyd, J. J.; Brothers, E.; Kudin, K. N.; Staroverov, V. N.; Kobayashi, R.; Normand, J.; Raghavachari, K.; Rendell, A.; Burant, J. C.; Iyengar, S. S.; Tomasi, J.; Cossi, M.; Rega, N.; Millam, J. M.; Klene, M.; Knox, J. E.; Cross, J. B.; Bakken, V.; Adamo, C.; Jaramillo, J.; Gomperts, R.; Stratmann, R. E.; Yazyev, O.; Austin, A. J.; Cammi, R.; Pomelli, C.; Ochterski, J. W.; Martin, R. L.; Morokuma, K.; Zakrzewski, V. G.; Voth, G. A.; Salvador, P.; Dannenberg, J. J.; Dapprich, S.; Daniels, A. D.; Farkas, Ö.; Foresman, J. B.; Ortiz, J. V.; Cioslowski, J.; Fox, D. J. *Gaussian09*; Gaussian, Inc.: Wallingford, CT, 2009.
(23) Hehre, W. J.; Ditchfield, R.; Pople, J. A. *J. Chem. Phys.* **1972**, *56*, 2257−2261.
(24) Hay, P. L.; Wadt, W. R. *J. Chem. Phys.* **1985**, *82*, 270−283.